Materials Horizons

OPINION

View Article Online
View Journal | View Issue

Cite this: *Mater. Horiz.*, 2025, 12, 7636

Received 9th April 2025,
Accepted 6th June 2025

DOI: 10.1039/d5mh00656b

rsc.li/materials-horizons

Mitigating the P2–O2 phase transition-induced structural instability in P2-$Na_x[Ni_{1/3}Mn_{2/3}]O_2$ Na-ion battery cathodes: to dope or not to dope, that is the question†

Mohamed H. Hassan, Jintao Fu, Jiaxin Liu and Eric Detsi*

To achieve high specific capacities in sodium-ion batteries (SIBs) containing P2-type $Na_{2/3}[Ni_{1/3}Mn_{2/3}]O_2$ (NNMO) cathodes, researchers have increasingly explored cycling batteries beyond the conventional 2–4 V voltage range. However, crossing this voltage boundary at either the upper or lower limits causes phase transitions that result in structural instability. This opinion article primarily focuses on the performance of NNMO in the higher voltage region, where P2–O2 phase transition occurs (≥4.2 V *vs.* Na/Na^+). This transition is accompanied by metal oxide layer gliding and lattice oxygen loss, leading to structural degradation. Among the various strategies to mitigate this effect, NNMO doping has been shown to minimize structural degradation and reduce capacity fading to a certain extent. In this opinion article, we argue that regardless of the doping elements, doped-NNMO does not yield satisfactory results for practical applications. This raises the question of whether doping NNMO is the right approach to mitigate structural instability issues during the P2–O2 phase transition between 2 and 4.5 V. In this opinion article, we clarify some misconceptions about NNMO doping strategies in mitigating the P2–O2 phase transition. Finally, we discuss a strategy beyond doping that might help address the aforementioned issues.

Cycling $Na_{2/3}[Ni_{1/3}Mn_{2/3}]O_2$ beyond 4 V

Rechargeable lithium-ion batteries (LIBs) used in battery-powered electric vehicles (EVs) and grid-scale energy storage face a significant supply chain hurdle involving critical materials and elements such as graphite, lithium, cobalt, and nickel used in these batteries. The sourcing of these elements from foreign countries, often fraught with geopolitical risks, raises concerns beyond mere technological consideration. A straightforward solution to mitigate supply chain challenges is to recycle LIBs at the end of their service life. However, so far, only ≈30% of cathode materials can be successfully recovered from recycling LIB slurry electrodes.[1] A promising alternative solution is to explore battery technologies that do not rely heavily on critical elements. In this respect, rechargeable sodium-ion batteries (SIBs) have emerged as a transformative energy storage technology, relying on the remarkable abundance and uniform geographic distribution of sodium resources, which promise to revolutionize sustainable battery development. For this purpose, several SIB companies across the globe, including CATL (China), Faradion (U.K.), Altris (Sweden), Northvolt (Sweden), Natron Energy (U.S.), and TIAMAT (France) are already developing commercial SIBs. However, most of these companies only focus on electrode materials such as hard carbon as the anode (capacity: 200–300 mA h g^{-1}), Prussian white/blue (capacity: 160 mA h g^{-1}), O3-type layered oxide (capacity: 164 mA h g^{-1}), and $Na_3V_2(PO_4)_2F_3$ (97 mA h g^{-1}) as the cathodes. To transcend the current limitations of energy density of SIBs, diverse electrode materials that outperform existing commercialization technology need to be explored. One such material is a P2-type $Na_x[Ni_{1/3}Mn_{2/3}]O_2$ (abbreviated NNMO) cathode, which has a theoretical capacity in the range 173–259 mA h g^{-1}, depending on the value of x. Specifically, P2-NNMO demonstrates remarkable electrochemical versatility as it can deliver a theoretical gravimetric capacity of 173 mA h g^{-1} in the voltage window between 2 and 4.5 V *vs.* Na/Na^+, when 2/3 Na is reversibly intercalated in combination with Ni^{2+}/Ni^{4+} oxidation/reduction. P2-NNMO can even deliver a theoretical gravimetric capacity of 259 mA h g^{-1} in the voltage window between ≈1.3 and 4.5 V *vs.* Na/Na^+, when an additional 1/3 Na is reversibly intercalated. This elevated performance also stems from involving the Mn^{3+}/Mn^{4+} oxidation/reduction reaction between 1.3 and 2 V, in addition to the (de)intercalation of

---

Department of Materials Science and Engineering, University of Pennsylvania, Philadelphia, PA, 19104, USA. E-mail: detsi@seas.upenn.edu

† Electronic supplementary information (ESI) available. See DOI: https://doi.org/10.1039/d5mh00656b

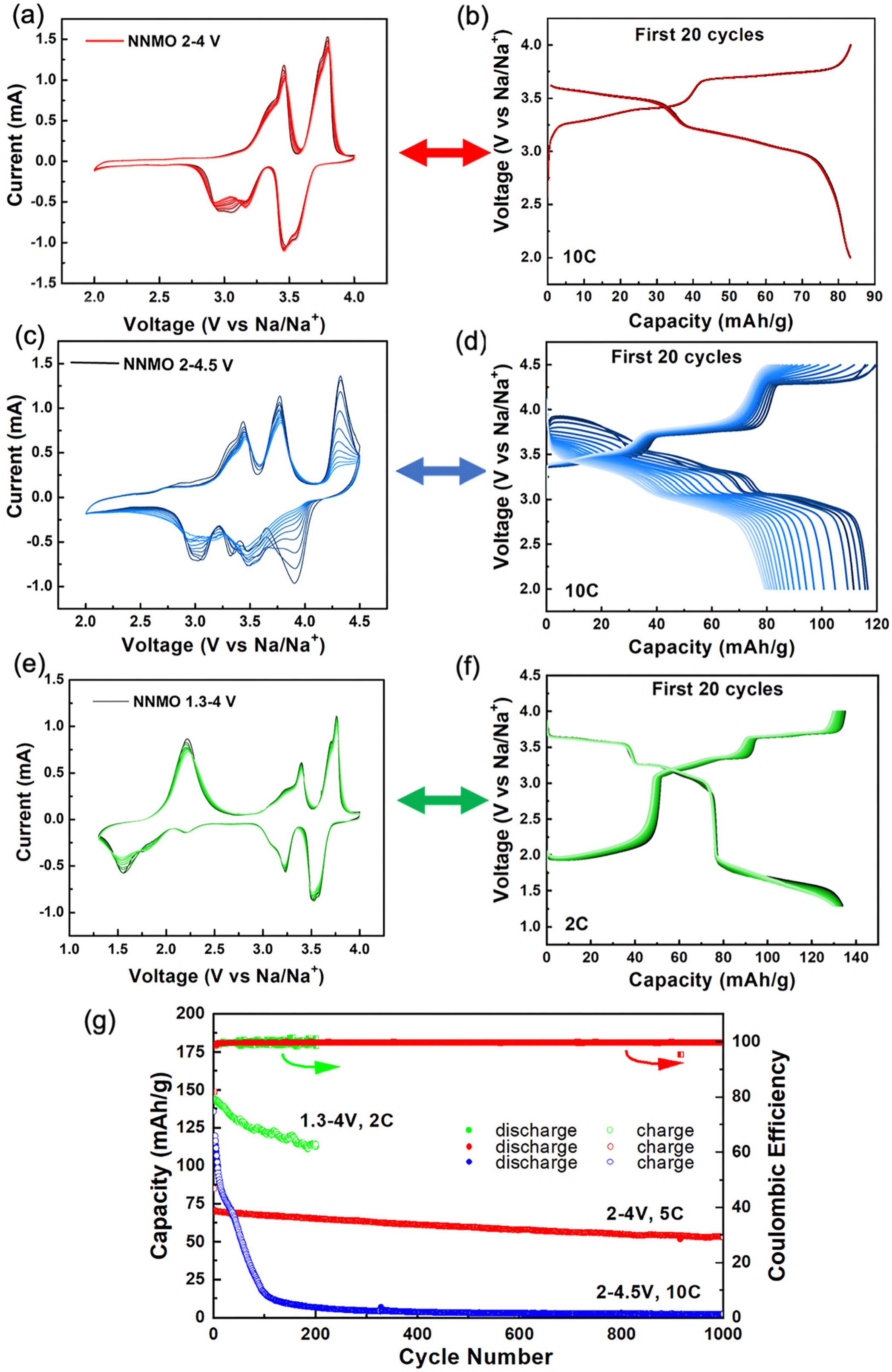

Fig. 1 (a) Cyclic voltammograms (CVs) of NNMO cycled in the 2–4 V window, (b) the corresponding galvanostatic cycling at 10C. (c) CVs of NNMO cycled at a higher voltage range of 2–4.5 V, (d) the corresponding galvanostatic cycling at 10C. (e) CVs of NNMO cycled in the region 1.3–4 V, (f) the corresponding galvanostatic cycling at 2C, and (g) long-term stability of NNMO cycled at different voltage ranges.

2/3 Na *via* Ni^{2+}/Ni^{4+} oxidation/reduction between 2 and 4.5 V. Practically, NNMO only cycles well in the voltage window between 2 and 4 V, where it delivers a relatively small capacity of 86 mA h g^{-1} when 1/3 Na is reversibly intercalated in combination with Ni^{2+}/Ni^{3+} oxidation/reduction. When NNMO is cycled at high voltage, it suffers from structural degradation during the P2–O2 phase transition occurring around 4.2 V. The degradation of this material results in rapid capacity fading within the first 10 cycles. Furthermore, expanding the operating voltage range below 2 V also results in poor cycling stability, possibly due to the Jahn–Teller distortion of Mn^{3+}. This distortion lowers the energy of the system and increases its degeneracy by elongating or compressing some bonds around the Jahn–Teller active elements.[2]

To optimize NNMO cathode performance, researchers have undertaken diverse strategies to mitigate the P2–O2 phase transition. Among these approaches, elemental doping has emerged as a compelling strategy, demonstrating potential for structural stabilization. However, despite the incremental progress, the performance of most doped NNMO does not meet the requirements for practical applications, such as a minimum lifespan of 1000 cycles. These demanding applications include portable electronics, electric vehicles, renewable energy storage, and grid storage. Indeed, one of the best cycle life values reported in the literature for doped NNMO (doping some Mn atoms with Fe atoms) operating between 2 and 4.5 V is only 300 cycles at 5C, with 85% capacity retention.[3] It is noteworthy that our research team attempted to reproduce these 300 cycles in Fe-doped NNMO with no success. So far, the community has struggled to demonstrate even 100 well-reproducible cycles in doped NNMO cycled between 2 and 4.5 V. For example, Zhang *et al.* reported 100 stable cycles in doped NNMO (substituting some Ni atoms with Fe atoms) operating between 2 and 4.2 V.[4] Our research team successfully reproduced their cell performance between 2 and 4.2 V. However, when we cycled the doped NNMO between 2 and 4.5 V, the cell suffered from a severe capacity loss within the first 10 cycles. On the other hand, Jiang *et al.* reported 100 stable cycles in doped NNMO (substituting some Ni atoms with Al atoms) operating between 2 and 4.3 V with 73% capacity retention.[5] Regardless of the doping element, doped-NNMO does not yield satisfactory results for practical applications. This raises the question of whether doping NNMO is an effective approach to mitigate issues related to material degradation at high voltages. This opinion article aims to comprehensively analyze the strategies of doping NNMO, outline the limitations of this approach, and propose a solution beyond doping for mitigating the phase transition issues.

P2–O2 transition in $Na_{2/3}[Ni_{1/3}Mn_{2/3}]O_2$

Na^+ can be reversibly intercalated in various P2 and O3 layered transition metal oxides (TMO) such as Na_xFeO_2, Na_xMnO_2, Na_xVO_2, Na_xCoO_2, and $Na_x[Ni_{1/3}Mn_{2/3}]O_2$, in which Na atoms reside in the trigonal prismatic (P) or octahedral (O) sites. The main difference between P2 and O3 structures lies within the number of TMO layers in the unit cell, represented by the number 2 or 3. In addition, these structures contain oxygen stacking sequences of ABBA for the P2-type and ABCABC for the O3-type.[6] The weak repulsive forces between the neighboring TMO layers enable various amounts (x) of sodium to be stored ($0 \leq x \leq 1$). Lee *et al.* demonstrated that the formation energy of the P2 phase is the lowest in the region $1/3 < x < 2/3$, while upon removing all Na ions ($x = 0$), the O2 phase is more stable. When $0 < x < 1/3$, both P2 and O2 phases coexist, leading to a long plateau at around 4.22 V.[7]

Fig. 1a shows 10 successive and stable cyclic voltammograms (CVs) of NNMO, which are recorded between 2 and 4 V *vs.* Na/Na^+ with the corresponding plot of the first 20 galvanostatic cycles shown in Fig. 1b. The two pairs of redox peaks from the CVs and the corresponding two pairs of plateaus from the galvanostatic plots are associated with the reversible storage of 1/3 Na *via* Ni^{2+}/Ni^{3+} redox, which yields a theoretical capacity of 86 mA h g^{-1}. The extraction/intercalation of Na is accompanied by Na^+/vacancy ordering transitions at various Na stoichiometries due to the repulsive Na^+–Na^+ forces. This reordering explains the presence of two pairs of redox peaks from the CV between 2 and 4 V, instead of one, for the Ni^{2+}/Ni^{3+} redox. It also justifies the corresponding voltage steps in the galvanostatic cycling curves between 2 and 4 V. On the other hand, Fig. 1c shows 10 rapidly decaying CVs of NNMO cycled between 2 and 4.5 V, with the corresponding plot of the first 20 galvanostatic cycles shown in Fig. 1d. There is an additional redox peak between 4 and 4.5 V observable in the CV, and a new plateau in the galvanostatic curve. This additional peak/plateau is associated with the reversible storage of the remaining 1/3 Na *via* Ni^{3+}/Ni^{4+} redox, yielding an additional theoretical capacity of 86 mA h g^{-1} and a total capacity of 173 mA h g^{-1} between 2 and 4.5 V. Furthermore, NNMO cycled in the voltage window 1.3–4 V (where it delivers a theoretical capacity of 173 mA h g^{-1} *via* Mn^{3+}/Mn^{4+} and Ni^{2+}/Ni^{3+} redox) showed a significantly slower capacity fading, as evidenced from the CVs and galvanostatic data shown in Fig. 1e and f, respectively. Finally, the red curve in Fig. 1g shows the excellent long-term stability and coulombic efficiency of NNMO cycled between 2 and 4 V, where we demonstrated 1000 cycles at 5C (current density 432.5 mA g^{-1}) with 76% capacity retention. In contrast, when cycled between 2 and 4.5 V, the initial capacity is relatively high (≈117 mA h g^{-1}), but the cell decays rapidly within the first 10 cycles and dies after 100 cycles, as shown by the blue curve in Fig. 1g. This premature cell death is a direct consequence of material degradation during the P2–O2 phase transition, a phenomenon initially elucidated through *in situ* X-ray diffraction experiments conducted by Dahn and his co-worker.[8] A graphical representation of P2/O2 NNMO chemical structures is shown at the unit cell level in Fig. 2a and b. The transition from P2 to O2 is accompanied by the sliding of oxygen layers in the unit cell, changing the stacking sequence from ABBA to ABAC and reducing the interlayer distance, leading to ≈20% volume change. Identifying the primary mechanism underlying the capacity degradation is critically important, as such

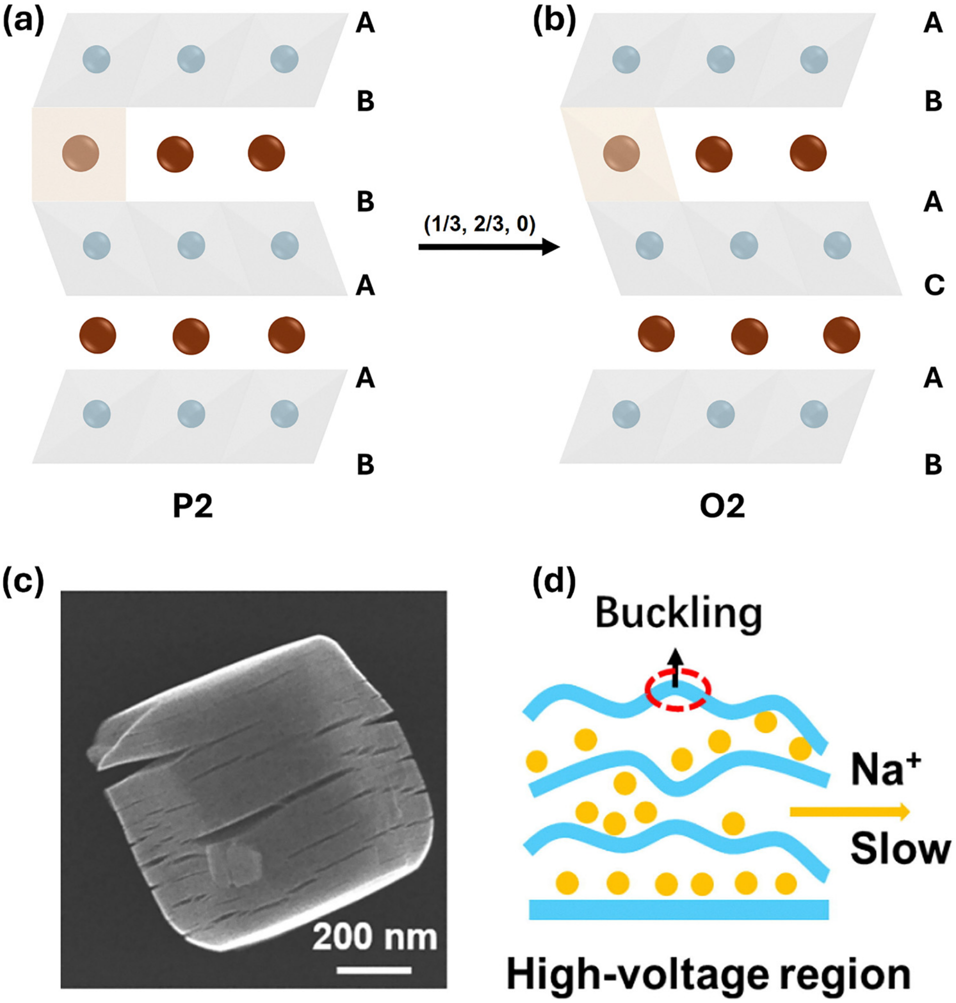

Fig. 2 Chemical structures of (a) P2 and (b) O2 phases of $Na_x[Ni_{1/3}Mn_{2/3}]O_2$. (c) SEM image of P2-NNMO particles, and (d) schematic illustration of the layered structure after cycling at high voltage showing the formation of cracks and crystal-plane buckling. (c) and (d) Were reproduced with permission from Elsevier.[5]

fundamental insights will enable the strategic development of targeted mitigation protocols. At the NNMO particle level (Fig. 2c and d), Jiang *et al.* demonstrated that the transition from P2 to O2 is accompanied by intergranular fracture of NNMO particles, which impedes Na extraction/insertion, resulting in rapid capacity fading within the first couple of cycles.[5] This research team showed that fractured NNMO particles (Fig. 2c) can still be (de)sodiated but at a higher overpotential, which suggests that capacity fading is primarily caused by the difficulty of inserting/removing Na in/from these fracture particles. In other words, the oxygen evolution often observed in NNMO cycled at a high voltage might not be the primary cause of capacity fading.

Controversy on the charge storage mechanism in P2-NNMO

In the voltage range of 2–4 V, one would anticipate the appearance of a single pair of redox peaks in the CV and one plateau in the galvanostatic curves due to Ni^{2+}/Ni^{3+} redox that is associated with the (de)intercalation of 1/3 of Na in/from NNMO. However, the CV of NNMO reveals two prominent pairs of redox peaks centered around 3.3 and 3.7 V *vs.* Na/Na^+, and two characteristic plateaus in the galvanostatic curves. The origin of these two pairs of redox peaks has been controversial. Some researchers attribute their presence to the Ni^{2+}/Ni^{3+} redox and Na^+/vacancy ordering,[4,7,9] while others assign them to Ni^{2+}/Ni^{3+} (for the 1st pair of redox peaks centered around 3.3 V *vs.* Na/Na^+), and Ni^{3+}/Ni^{4+} (for the 2nd pair of redox peaks centered around 3.7 V *vs.* Na/Na^+).[10,11] In this section, we aim to clarify why we believe that the two pairs of redox peaks are intricately linked to Ni^{2+}/Ni^{3+} in combination with Na^+/vacancy ordering, while Ni^{3+}/Ni^{4+} exists only at a higher voltage.

The 1st pair of redox peaks initially emerges at a lower voltage (3.3 V *vs.* Na/Na^+) upon the (de)intercalation of 1/6 of Na atoms in combination with partial Ni^{2+}/Ni^{3+} redox. However, due to Na^+/vacancy ordering occurring during the process, it becomes more difficult to further (de)intercalate Na at this voltage (3.3 V *vs.* Na/Na^+), causing further (de)intercalation of

Na to take place at a relatively higher voltage (3.7 V *vs.* Na/Na^+). This gives rise to the 2nd pair of redox peaks during the (de)intercalation of the remaining 1/6 of Na and full Ni^{2+}/Ni^{3+} redox. Na^+/vacancy ordering is prevalent in P2-type layered oxides containing more than one transition metal (TM), particularly when the Fermi levels of these TMs are closely aligned.[12,13] However, when TM Fermi levels are different, the electronic delocalization and Na^+/vacancy ordering are broken. This inhibition results in better Na^+ mobility and a single plateau on the charge/discharge curves (or a single pair of redox peaks on the CV). Thus, the presence or absence of ordered intermediate phases directly influences whether steps in the voltage profiles appear. Wang *et al.* have modified the structure of NNMO *via* Ti doping, as Ti has a significantly different Fermi level than Mn, leading to the disappearance of Na^+/vacancy ordering and its associated step in the voltage plateau along with obtaining a featureless CV.[12] Additionally, Lee *et al.* have demonstrated the appearance and disappearance of the 2θ peaks between 7 and 8° during NNMO cycling (λ = 0.413 Å), as they were ascribed to Na^+/vacancy superstructure ordering, as shown in Fig. 3a.[7] To explain the voltage step associated with Na rearrangements shown in Fig. 3b, let us consider the progression of Na content during cycling, as shown in eqn (1), where two major intermediate phases can be identified at approximately 3.3 and 3.7 V.[14]

$$\begin{aligned} Na_{\frac{2}{3}}Ni_{\frac{1}{3}}Mn_{\frac{2}{3}}O_2 &\overset{\frac{1}{6}\text{Na, 3.3 V}}{\longleftrightarrow} Na_{\frac{1}{2}}Ni_{\frac{1}{3}}Mn_{\frac{2}{3}}O_2 \\ &\overset{\frac{1}{6}\text{Na, 3.7 V}}{\longleftrightarrow} Na_{\frac{1}{3}}Ni_{\frac{1}{3}}Mn_{\frac{2}{3}}O_2 \qquad (1) \\ &\overset{\frac{1}{3}\text{Na, 4.2 V}}{\longleftrightarrow} Ni_{\frac{1}{3}}Mn_{\frac{2}{3}}O_2 \end{aligned}$$

In pristine NNMO, 2/3 Na occupies two types of trigonal prismatic sites: the face-sharing sites (Na_f) and the edge-sharing sites (Na_e) relative to the TMO_6 octahedrons. The arrangement of Na ions within these sites occurs in a way that minimizes the electrostatic repulsion and stabilizes the structure. Notably, Meng *et al.* have identified a unique pattern where Na_f forms a "large zigzag" (LZZ) configuration with the distance between Na_f ions equivalent to $2a_{hex}$, Fig. 3c.[15] During charging, the first step involves the removal of 1/6 of Na ions and the oxidation of 1/6 of Ni^{2+} ions. The remaining 1/2 Na ions then rearrange in alternating rows, with each Na_f row positioned between two Na_e rows. Simultaneously, an intermediate phase $Na_{1/2}Ni_{1/3}Mn_{2/3}O_2$ forms, characterized by a voltage step at 3.3 V, Fig. 3b. The subsequent transition follows a similar trend, leaving 1/3 Na ions in the structure while achieving complete oxidation of Ni^{2+} to Ni^{3+}. Here, Na rearranges into rows occupying either Na_f or Na_e sites, giving rise to $Na_{1/3}Ni_{1/3}Mn_{2/3}O_2$ and a second voltage step at 3.7 V. At this stage, the obtained capacity is about 86 mA h g^{-1}, while an additional 86 mA h g^{-1} can be attained when NNMO is cycled up to 4.5 V. During this final stage, the remaining 1/3 Na ions are removed, accompanied by the complete oxidation of Ni^{3+} to Ni^{4+}.

Current doping strategies to overcome issues related to the P2–O2 transition

In recent years, significant efforts have been made to develop strategies to mitigate the detrimental P2–O2 phase transition and cathode–electrolyte side reactions at high voltage. Strategies such as elemental doping (with a transition metal, alkaline earth metal, or alkali metal), coating the surface of cathode particles, selecting the right type of binder, *etc.*, have been reported in numerous articles.[16–20] Among them, elemental doping is the most extensively explored strategy to cycle NNMO beyond the 2–4 V limit. One of the primary objectives of this approach is to stabilize the P2 structure and break the aforementioned Na^+/vacancy ordering. This is achieved by introducing foreign transition metal elements with similar ionic radii but different Fermi levels into the TM layers of NNMO.[20] Recently, the scope of elemental doping has been expanded to encompass the partial replacement of Na ions in NNMO.[21] Moreover, a multi-ion doping strategy has emerged to further enhance NNMO stabilization. This approach not only synergistically combines the positive effect of single-ion doping but also introduces additional cooperative behavior.[17,18] Fig. 4a provides a concise overview of the elements used in NNMO doping. Despite the shared objective of these strategies in stabilizing the P2 structure, the underlying mechanisms diverge based on the specific elements and their doping location. This section will highlight some of the key achievements while also discussing their effectiveness and limitations.

Na site doping

In this strategy, some Na atoms are substituted by alkali or alkaline earth metals, as illustrated in Fig. 4a (blue). Strategies to unlock NNMO's full capacity and cycle life include prohibiting the participation of oxygen anions in the charge transfer process and increasing the sodium content in the material. Given that the P2–O2 phase transition occurs when the sodium content falls below 33 at%, a promising methodology involves synthesizing cathode materials with inherently high sodium content. Such an approach could potentially expand the working potential window beyond 4 V without breaching the critical 33 at% critical limit. In a notable study, Ma *et al.* prepared a high Na-content and TM-deficient P2-$Na_{0.78}Ni_{0.23}Mn_{0.69}O_2$ that exhibited a commendable reversible capacity of 138 mA h g^{-1} while maintaining structure integrity when cycled between 2 and 4.5 V.[11] The charge compensation primarily relied on the redox couple Ni^{2+}/Ni^{4+}, with no significant contribution from Mn^{4+} within the bulk of the material. However, their in-depth characterization revealed the presence of trace amounts of Mn^{3+} and an oxidation state gradient of the TM species from the surface to the bulk of the cycled particle. This gradient is closely associated with the formation of oxygen vacancies at the particles' surface. The surface densification as a result of the generated oxygen vacancies has been visualized in NNMO by means of high-resolution microscopy.[4] We believe that if this work included a quantitative measurement of the Na content above 4 V, it would give better insight into the importance of

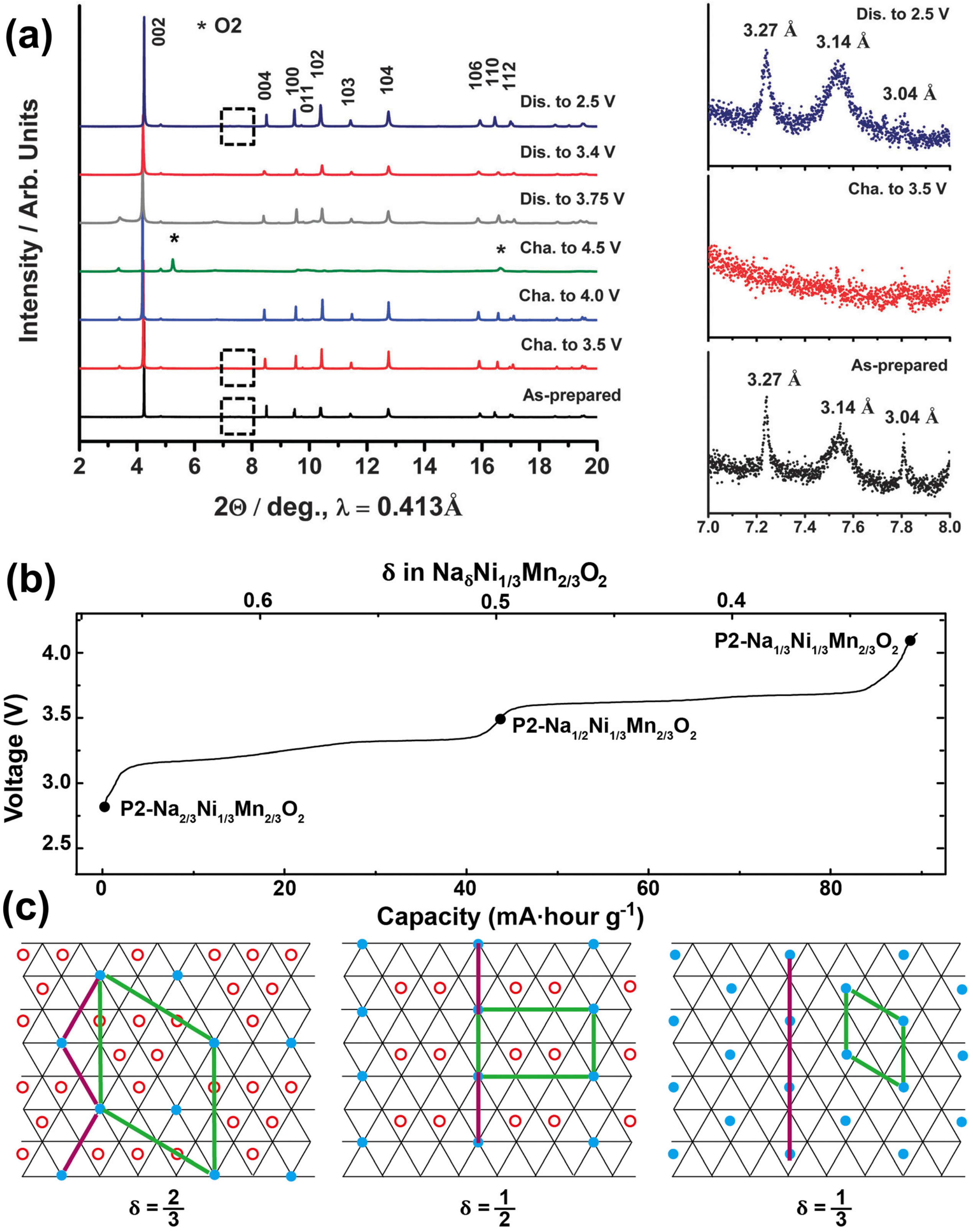

Fig. 3 (a) XRD patterns of NNMO at different charge/discharge states (left) and the corresponding enlarged areas (right) reflecting Na^+/vacancy superstructure ordering. Reproduced with permission from the Royal Society of Chemistry.[7] (b) Charge/discharge profile of NNMO showing the two plateaus related to the rearrangement of Na^+/vacancy ordering. (c) Schematic illustration demonstrating Na^+/vacancy ordering in $Na_\delta Ni_{1/3}Mn_{2/3}O_2$ at different Na content levels (δ): red circles represent Na^+ at Na_e sites while blue ones represent Na^+ at Na_f sites. Green lines represent the unit cell. Reproduced with permission from the American Association for the Advancement of Science.[12]

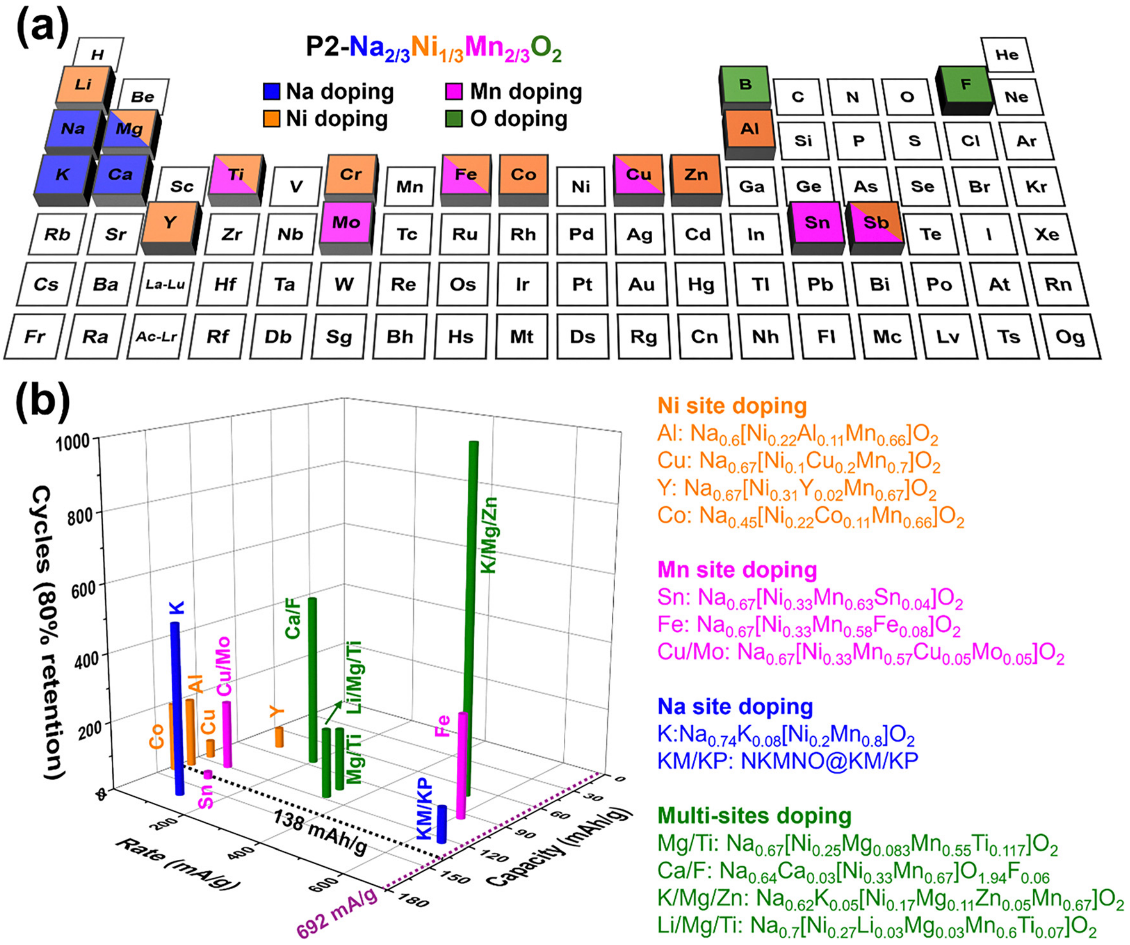

Fig. 4 (a) Periodic table summarizing the elements that can be doped into NNMO. (b) Comparison of cycling performance for modified NNMO electrodes based on Ni site doping (orange), Mn site doping (magenta), Na site doping (blue), and multi-ion doping (green). Industrial targets of achieving 80% nominal capacity in 15 min are indicated by dashed black (138 mA h g^{-1}) and dashed purple (692 mA g^{-1}) lines, respectively.

higher sodium content at high voltage in cathode materials. In addition, a higher number of cycles needed to be presented to indicate the long-term stability of this material.

Instead of attempting to suppress the phase transition, Wang *et al.* used an alternative strategy by doping the alkali ion layer with K ions.[21] They synthesized O–P2 $K_{0.4}[Ni_{0.2}Mn_{0.8}]O_2$ considering that K ions would not participate in the charge transfer process during cycling and would instead stay in the alkali ion layer permanently. The presence of K ions supported the transition metal layer when sodium was almost completely extracted, bypassing the 33% Na content limit. During cycling, this cathode became sodiated reaching the formula $K_{0.08}Na_{[0-0.74]}[Ni_{0.2}Mn_{0.8}]O_2$ and transitioning between four states. Some of the leached K ions formed KPF_6 in the electrolyte, while others were deposited on the anode. When cycled between 1.5 and 4.2 V, this material delivered a capacity of 194 mA h g^{-1} at 0.1C and retained 86% of its capacity after 500 cycles at 1C. Their detailed examination revealed that the anions in the cathode did not participate in any electrochemical processes. Although this study provided an alternative route to increase NNMO capacity, when cycled up to 4.5 V, the structure collapsed. In addition, cycling this type of material below 2 V led to Jahn–Teller distortions in the MnO_6 polyhedra, demonstrated in this study by the presence of two different Mn–O bond lengths. From our experience, the structural degradation due to the Jahn–Teller distortions is slower than the one due to P2–O2 transitions, as has been demonstrated previously in Fig. 1e and f.

The idea of alkali metal ion doping is extended to include the formation of a protective coating around K-doped-NNMO particles. The K ionic radius is larger than Na ionic radius, thus promoting Na ion diffusion and increasing the rate performance of the doped material. Coupling that with their stabilizing effects, protective coating solutions present a new frontier for enhancing the overall cathode performance. The P2-$Na_{0.67}[Ni_{0.25}Mn_{0.75}]O_2$ layered oxide cathode material has been doped with K as well as coated with a birnessite-like $K_2Mn_4O_8$ film formed *in situ*.[22] This cathode demonstrated a specific capacity of ≈124 mA h g^{-1} when cycled at 5C in the voltage window 1.5–4 V with a 90.1% capacity retention after 100 cycles. Since the material was cycled below 2 V, we always recommend probing the formation of Mn^{3+} and the possible changes in the Na/Ni/Mn content at different states of charge.

Other works include the substitution of some sodium and oxygen anions with Ca ions and F ions, respectively, to help stabilize the layered structure at high voltages.[23] When P2-$Na_{0.67-x}Ca_x[Ni_{0.33}Mn_{0.67}]O_{2-2x}F_{2x}$ was cycled at low current rates in the voltage range of 2–4.3 V, an obvious decay in the capacity was observed. When cycled at 10C, it delivered a capacity of $\approx$49 mA h g^{-1}, which was significantly lower than the expected capacity of NNMO cycled at this rate. Even when cycled at 1C for an extended period (500 cycles), the material did not demonstrate any significant increase in the capacity compared to the numbers reported for undoped NNMO. Li has also been used to substitute Na in several reports, where the inclusion of Li mitigated the phase transition, allowing a high-capacity Na-containing cathode.[24] Although many reports have demonstrated the inclusion of Li atoms within the TMO layer (replacing Mn or Ni), an in-depth study on $Na_x[Ni_{0.22}Li_{0.12}Mn_{0.66}]O_2$ showed that Na/Li ions diffuse between the layers at different stages of (dis)charge.[25] Here, ^{7}Li solid-sate NMR revealed the presence of a large number of Li resonances assigned to various sites in the TMO layers and in the interlayer space with no evidence for TMO layer gliding below 4.4 V. These Li ions migrated reversibly from the TMO layers to the interlayer space at high voltage. Despite the impressive performance of such cathode materials, the idea of including Li in the synthesis contradicts the purpose of developing SIBs to avoid the geopolitical risks associated with the Li metal. The cycling performance of selected Na-doped NNMO is summarized in blue in Fig. 4b, a graph that juxtaposes the cycling performance using key metrics, including initial reversible capacity, rate capability, and cycle life. One can conclude that K ions are the most suitable for substituting Na in a NNMO layered structure. K doping has been shown to successfully increase the specific capacity and cycling stability of NNMO *via* postponing the P2–O2 phase transition.

Ni site doping

To date, various types of alkali metals, alkaline earth metals, and transition metals have been investigated as NNMO dopants to replace Ni atoms, as summarized in Fig. 4a (orange). For instance, Ni has been partially substituted with Li to make cathode materials such as $Na_{0.8}[Ni_{0.22}Li_{0.12}Mn_{0.66}]O_2$, where Li migrates to Na sites when charged at high voltage and effectively prevents the undesirable layer gliding, delivering a reversible capacity of about 115 mA h g^{-1} up to 50 stable cycles, when cycled between 2 and 4.4 V *vs.* Na/Na^+.[26] Substituting some Ni atoms with Mg can trigger the reversible P2–OP4 phase transition, where the OP4 phase is an intergrowth of P2 and O2, thus mitigating the capacity decay to some extent.[27,28] For example, the $Na_{0.67}[Ni_{0.2}Mg_{0.1}Mn_{0.7}]O_2$ system having a reversible P2–OP4 transformation delivered $\approx$120 mA h g^{-1} for 50 cycles, when cycled between 2 and 4.5 V.[27] Interestingly, the mobility of Na ions measured by the galvanostatic intermittent titration technique (GITT) showed 2 orders of magnitude improvement compared to the undoped NNMO. This enhanced performance was justified by the fact that part of the Ni atoms are replaced by larger Mg atoms, leading to an enhanced interlayer spacing.[29] Zn and Al have also been used to substitute Ni atoms such as in $Na_{0.66}[Ni_{0.26}Zn_{0.07}Mn_{0.67}]O_2$[30] and $Na_{0.6}[Ni_{0.22}Al_{0.11}Mn_{0.66}]O_2$,[31] respectively, which improved their cycling stability. For example, a capacity retention of $\approx$102 mA h g^{-1} after 200 cycles has been demonstrated in $Na_{0.6}[Ni_{0.22}Al_{0.11}Mn_{0.66}]O_2$ when cycled between 2 and 4.3 V.[31] In the above examples, dopant atoms are electrochemically inactive, thus sacrificing the capacity. Doping NNMO with electrochemically active atoms has also been proposed. Among them, Cu and Fe dopants exhibit a comparable reversible P2–OP4 transition as with the case of Mg discussed earlier. Maintaining a Cu concentration threshold of approximately 20% (*i.e.*, $Na_{0.67}[Ni_{0.1}Cu_{0.2}Mn_{0.7}]O_2$) ensures the persistence of the P2 structure across the entire voltage range without undergoing the OP4 phase, yielding a capacity of $\approx$104 mA h g^{-1} after 50 cycles in the voltage range between 2 and 4.5 V.[32–34] Substituting Ni atoms with Co in $Na_{0.45}[Ni_{0.22}Co_{0.11}Mn_{0.66}]O_2$ can expand the interlayer spacing and enhance the electronic conductivity, leading to a high reversible capacity of $\approx$119 mA h g^{-1} after 100 cycles between 2.1 and 4.3 V.[35] The cycling performance of selected Ni-doped NNMO is summarized in orange in Fig. 4b.

Mn site doping

In this strategy, a fraction of Mn atoms is substituted by a variety of elements, such as Sn and Sb, as illustrated in Fig. 4a (pink). Ti doping in $Na_{0.67}[Ni_{0.33}Mn_{0.5}Ti_{0.17}]O_2$ was used to mitigate the volume change associated with P2–O2 transition from >20% to $\approx$12%, yielding a capacity of $\approx$112 mA h g^{-1} after 20 cycles when cycled between 2.5 and 4.5 V.[36] Fe-doped NNMO, such as in $Na_{0.67}[Ni_{0.33}Mn_{0.58}Fe_{0.08}]O_2$ delivered a capacity of $\approx$80 mA h g^{-1} after 300 cycles at 5C when cycled between 2.2 and 4.4 V.[3] Sn doping in $Na_{0.67}[Ni_{0.33}Mn_{0.63}Sn_{0.04}]O_2$ takes advantage of the strong Sn–O bond to suppress the gliding of TMO layers, yielding a high initial capacity of $\approx$138 mA h g^{-1} when cycled between 2 and 4.3 V, but this capacity dropped to $\approx$78 mA h g^{-1} after 100 cycles ($\approx$57% retention).[37] The cycling performance of selected Mn-doped NNMO is summarized in Fig. 4b,[3,37,38] where it is seen that the rate performance is generally better compared to Ni-doped NNMO. However, cycle life above 300 cycles is hardly achieved.

Multi-ion doping

Multi-ion doping combines the advantages of single-element doping introduced above in one cathode material. For instance, $Na_{0.67}[Ni_{0.25}Mg_{0.083}Mn_{0.55}Ti_{0.117}]O_2$ takes advantage of substituting some Na atoms with Mg to break the Na^+/vacancy ordering while partially substituting Mn atoms with Ti to suppress the ''delocalization'' of Mn–O layers.[39] It should be noted that in this case, Mg will first occupy Ni sites prior to diffusing to Na sites at a higher concentration. The resulting structure delivered $\approx$90 mA h g^{-1} after 100 cycles when cycled between 3 and 4.4 V. Similarly, by doping NNMO *via* the partial substitution of Na and O, $Na_{0.64}Ca_{0.03}[Ni_{0.33}Mn_{0.67}]O_{1.94}F_{0.06}$ can deliver $\approx$75 mA h g^{-1} after 500 cycles when cycled between 2 and 4.3 V, as discussed in the previous section.[23] Doping with more than one element to replace Mn atoms has also been explored. For instance, $Na_{0.67}[Ni_{0.33}Mn_{0.57}Cu_{0.05}Mo_{0.05}]O_2$ utilizes Cu to mitigate issues related to P2–O2 transition and Mo to inhibit Na^+/vacancy ordering, delivering a capacity of ≈ 125 mA h g^{-1} after 100 cycles when cycled between 2 and 4.5 V.[38] The cycling performance of selected multi-site doped NNMO is presented in Fig. 4b in green.[23,24,39,40] It can be seen that multi-ion doped NNMO generally exhibits superior rate performance and cycle life compared to the single-ion doped ones. Notably, some of them (*i.e.*, $Na_{0.62}K_{0.05}[Ni_{0.17}Mg_{0.11}Zn_{0.05}Mn_{0.67}]O_2$) can achieve the targeted 1000 cycles with 80% capacity retention, but with a lowered capacity than anticipated.

As discussed previously, Na-site doping has the advantage of boosting Na^+ diffusion, leading to better rate performance (*i.e.*, in the case of doping with K), while some dopants (*e.g.*, Li) may raise concerns as a critical element. Transition metal layer doping in Ni and Mn sites has the advantage of offering a wide selection of dopants, as shown in Fig. 4a. However, some of these doping strategies bring a trade-off with lowered capacity due to their electrochemical inactivity. Lastly, multi-ion doping brings together the advantages of each single-site doping while introducing additional synergetic benefits, resulting in their generally improved performance as shown in Fig. 4b. Despite these advancements, significant performance gaps persist with the current state-of-the-art doping strategies, limiting their comprehensive effectiveness and potential for widespread application.

To summarize, elemental doping has been extensively investigated as a strategy to mitigate the P2–O2 phase transition that limits high-voltage operation (≥ 4.2 V *vs.* Na/Na^+). Various doping methods, including those involving Na, Ni, and Mn sites, as well as multi-ion doping, have demonstrated the potential to enhance cycling stability and capacity by suppressing this transition. Na-site doping aims to stabilize the structure at higher voltages by maintaining high sodium content or incorporating alkali–metal ions, while Ni-site doping utilizes substituent ions to enhance structural integrity or improve Na^+ mobility, often at the cost of capacity. Mn-site doping focuses on suppressing volume change and layer gliding to improve rate performance, but capacity retention can be a concern. Multi-ion doping seeks to synergistically integrate the benefits of these individual approaches, usually demonstrating improved overall performance by targeting multiple instability mechanisms, yet a balance between capacity and cycle life remains a key challenge. Despite the progress made with various doping strategies, further enhancements are still needed to fully address the performance limitations by the P2–O2 transition for practical application in Na-ion batteries.

Is there another way to mitigate the phase transition issue?

While phase transition in cathode materials has predominantly been investigated in periodic bulk systems near equilibrium, investigations in nanomaterials remain remarkably limited. Phase stability of anatase and rutile titania nanoparticles has been demonstrated to be highly sensitive to particle size. In this system, below a critical size of around 14 nm, the total free energy of rutile is higher, and anatase becomes more stable.[41] In a different system, Bia *et al.* proposed a theory of reaction-limited intercalation in $LiFePO_4$ nanoparticles, where the model predicted that the suppression of phase separation can occur above a critical current.[42] Furthermore, experimental observation revealed that as the size of $LiFePO_4$ crystals decreases, the miscibility gap between Li-rich and Li-poor phases during cycling diminishes significantly.[43] The mechanism behind this phenomenon has been attributed to the nanoconfinement of the interphase boundary and the stabilization of the ion concentration gradient near the particle surface. In addition to cathodes, nanostructured anodes have garnered significant attention for their application in LIBs due to their superior cycling performance compared to their bulk counterparts. In our recent study, we investigated the size-dependent phase transformation pathways in Ag, which we used as a model alloy anode for LIBs. Our approach combined CALPHAD-based modeling and experimental studies.[44] As the active material particle size (r) decreases, the overall Gibbs free energy change ΔG_{GT} increases (Gibbs–Thomson effect), as shown in eqn (2). Here, γ and V_m are the surface energy and the molar volumes, respectively.

$$\Delta G_{GT} = 2\gamma V_m/r \qquad (2)$$

The increase in ΔG_{GT} alters the Ag–Li phase equilibria, resulting in the emergence of alternative phase transformation pathways in the nanostructured electrode material. Our studies revealed that, while the bulk Ag anode exhibited a voltage profile during cycling similar to the simulated data, the nanoporous Ag anode underwent phase transformations accompanied by the formation of a metastable β solid solution phase, as seen in Fig. 5. Moreover, the nanoporous Ag anode demonstrated improved mechanical stability during cycling in addition to the size-dependent Li solubility; both properties are essential in developing a high-capacity alloy anode.

Despite numerous studies that explore the particle size dependency on the anode/cathode performance in LIBs, comparable investigation for sodium-rich nanostructured cathodes remains scarce. Therefore, inspired by the aforementioned size dependency on the anode/cathode performance in LIBs, NNMO particle size reduction (below a critical value) might lead to a harmless P2–O2 phase transition and better mechanical stability of the particles upon cycling at high voltage. Following this approach to mitigate P2–O2 transition outcomes, Liu *et al.* explored the behavior of P2-NNMO porous nanofibers upon cycling at high (4.5 V) and low (1.5 V) voltage regions.[45] The synthesized nanofibers, which were assembled from smaller nanoparticles, exhibited both high rate capability and an enhanced cycle life in the voltage window of 1.5–4 V. Interestingly, when cycled up to 4.5 V, the CV curve and charge/discharge profiles displayed smoother peaks and plateaus compared to the bulk material. Additionally, a relatively

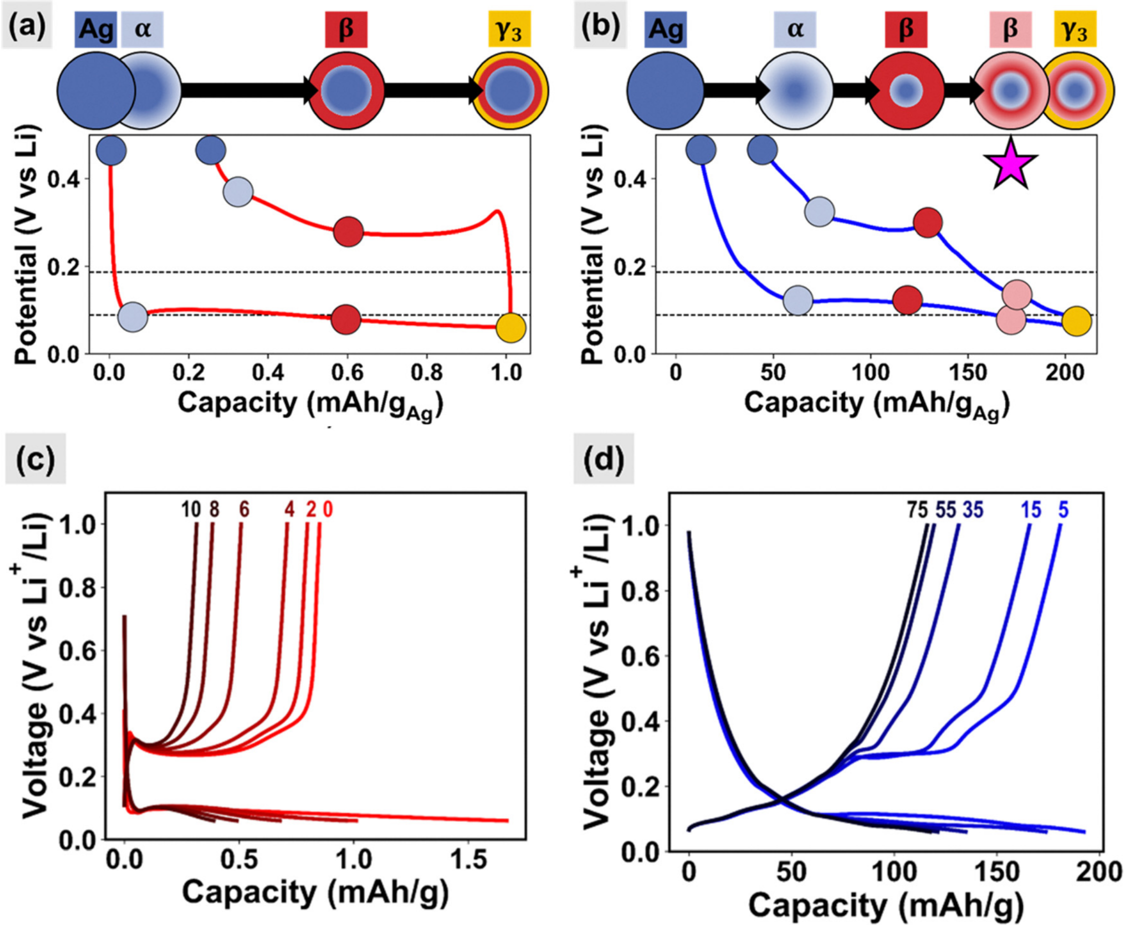

Fig. 5 Voltage profiles and the associated phase transformation in (a) and (c) bulk Ag and (b) and (d) nanoporous Ag anodes. The appearance of the nonequilibrium β solid solution phase in the nanoporous Ag is labelled with the pink star. Reproduced with permission from the American Chemical Society.[44]

stable 4.2 V voltage plateau was maintained during cycling, contributing to the improved cycle life. Although the enhanced performance has been attributed to the alleviated Na^+/vacancy ordering, other factors also contribute to stabilization. Specifically, the facilitated Na-ion diffusion and the mitigation of particle cracking due to size reduction played crucial roles in maintaining structural integrity. Nanostructuring is expected to improve the mechanical stability of the particles, rendering them more ductile rather than brittle. Consequently, reducing the particle size of NNMO to a certain extent could effectively mitigate particle cracking. This favorable outcome would facilitate rapid Na diffusion kinetics during high-voltage cycling, resulting in harmless P2–O2 reversible transitions. On the other hand, there are some disadvantages in using nanomaterials in energy storage systems originating from their difficulty of synthesis, the side reactions that happened due to the high surface area, increased interfacial resistance, and the reduced volumetric energy density.[46] When it comes to the synthesis of nano-NNMO, the synthetic conditions might pose challenges in obtaining the desired phase in the target size range. First, the synthesis is performed at 800–950 °C in air, this high temperature range and the presence of oxygen lead to either coarsening of the particles, or the formation of competing phases (*e.g.*, spinel Mn_3O_4 or rock-salt NiO). In addition, if the temperature is not optimized, other phases of NNMO can easily form, such as the P3 phase. That is why innovative methods need to be adopted for the precise synthesis of phase pure NNMO nanoparticles.

Concluding remarks

In summary, this opinion article discusses the widespread use of doping to address the structural degradation in P2-type $Na_{2/3}[Ni_{1/3}Mn_{2/3}]O_2$ (NNMO) cathodes for Na-ion batteries, which leads to capacity fading when cycled beyond 4 V *versus* Na/Na^+. We first present experimental data demonstrating the excellent cycling performance of P2-NNMO within the voltage range of 2–4 V *versus* Na/Na^+. However, it shows rapid capacity fading when cycled above 4 V *versus* Na/Na^+. Next, we delve into the fundamental mechanisms associated with the P2–O2 phase transition in NNMO, and we also address the ongoing controversy regarding the charge storage mechanism in this material. Finally, we review various doping strategies aimed at overcoming the issues related to the P2–O2 phase transition, including Na site doping, Ni site doping, Mn site doping, and multi-ion doping. While these doping strategies show some promise in minimizing structural degradation and reducing capacity fading, the results remain unsatisfactory for practical applications. Regardless of the doping element used, current strategies do not fully resolve the material's degradation during the P2–O2 phase transition. To address these challenges, we believe that the scientific community should explore alternatives to doping, such as significantly reducing the size of NNMO through nanostructuring, which may fundamentally suppress the P2–O2 phase transition.

Conflicts of interest

The authors declare no conflicts of interest.

Data availability

The data supporting this article have been included in the main manuscript.

Acknowledgements

The authors gratefully acknowledge the financial support from the National Science Foundation (NSF), Division of Materials Research (DMR), Future Manufacturing Research Grant #2134715 (E. D.). The authors express their gratitude to Stella Lin for her meticulous proofreading of the manuscript.

References

1 X. Ma, M. Chen, Z. Zheng, D. Bullen, J. Wang, C. Harrison, E. Gratz, Y. Lin, Z. Yang, Y. Zhang, F. Wang, D. Robertson, S.-B. Son, I. Bloom, J. Wen, M. Ge, X. Xiao, W.-K. Lee, M. Tang, Q. Wang, J. Fu, Y. Zhang, B. C. Sousa, R. Arsenault, P. Karlson, N. Simon and Y. Wang, *Joule*, 2021, **5**, 2955–2970.

2 X. Li, X. Ma, D. Su, L. Liu, R. Chisnell, S. P. Ong, H. Chen, A. Toumar, J.-C. Idrobo, Y. Lei, J. Bai, F. Wang, J. W. Lynn, Y. S. Lee and G. Ceder, *Nat. Mater.*, 2014, **13**, 586–592.

3 Q. Yang, P.-F. Wang, J.-Z. Guo, Z.-M. Chen, W.-L. Pang, K.-C. Huang, Y.-G. Guo, X.-L. Wu and J.-P. Zhang, *ACS Appl. Mater. Interfaces*, 2018, **10**, 34272–34282.

4 Y. Zhang, M. Wu, J. Ma, G. Wei, Y. Ling, R. Zhang and Y. Huang, *ACS Cent. Sci.*, 2020, **6**, 232–240.

5 M. Jiang, G. Qian, X.-Z. Liao, Z. Ren, Q. Dong, D. Meng, G. Cui, S. Yuan, S.-J. Lee, T. Qin, X. Liu, Y. Shen, Y.-S. He, L. Chen, Y. Liu, L. Li and Z.-F. Ma, *J. Energy Chem.*, 2022, **69**, 16–25.

6 C. Delmas, C. Fouassier and P. Hagenmuller, *Physica B+C*, 1980, **99**, 81–85.

7 D. H. Lee, J. Xu and Y. S. Meng, *Phys. Chem. Chem. Phys.*, 2013, **15**, 3304–3312.

8 Z. Lu and J. R. Dahn, *J. Electrochem. Soc.*, 2001, **148**, A1225.

9 S. Liu, J. Wan, M. Ou, W. Zhang, M. Chang, F. Cheng, Y. Xu, S. Sun, C. Luo, K. Yang, C. Fang and J. Han, *Adv. Energy Mater.*, 2023, **13**, 2203521.

10 C. Zhao, Z. Yao, Q. Wang, H. Li, J. Wang, M. Liu, S. Ganapathy, Y. Lu, J. Cabana, B. Li, X. Bai, A. Aspuru-Guzik, M. Wagemaker, L. Chen and Y.-S. Hu, *J. Am. Chem. Soc.*, 2020, **142**, 5742–5750.

11 C. Ma, J. Alvarado, J. Xu, R. J. Clément, M. Kodur, W. Tong, C. P. Grey and Y. S. Meng, *J. Am. Chem. Soc.*, 2017, **139**, 4835–4845.

12 P. F. Wang, H. R. Yao, X. Y. Liu, Y. X. Yin, J. N. Zhang, Y. Wen, X. Yu, L. Gu and Y. G. Guo, *Sci. Adv.*, 2018, **4**, eaar6018.

13 Y. Wang, R. Xiao, Y.-S. Hu, M. Avdeev and L. Chen, *Nat. Commun.*, 2015, **6**, 6954.

14 J. Mao, X. Liu, J. Liu, H. Jiang, T. Zhang, G. Shao, G. Ai, W. Mao, Y. Feng, W. Yang, G. Liu and K. Dai, *J. Electrochem. Soc.*, 2019, **166**, A3980.

15 Y. S. Meng, Y. Hinuma and G. Ceder, *J. Chem. Phys.*, 2008, **128**, 104708.

16 H. Jiang, G. Qian, R. Liu, W.-D. Liu, Y. Chen and W. Hu, *Sci. China Mater.*, 2023, **66**, 4542–4549.

17 J. Xiao, Y. Xiao, J. Li, C. Gong, X. Nie, H. Gao, B. Sun, H. Liu and G. Wang, *SmartMat*, 2023, **4**, e1211.

18 B. Peng, G. Wan, N. Ahmad, L. Yu, X. Ma and G. Zhang, *Adv. Energy Mater.*, 2023, **13**, 2300334.

19 L. Chang, R. Yang, X. Bi, W. Yang, K. Cai, A. Wei and J. Liu, *J. Energy Storage*, 2023, **73**, 109025.

20 J. Zhang, W. Wang, W. Wang, S. Wang and B. Li, *ACS Appl. Mater. Interfaces*, 2019, **11**, 22051–22066.

21 Y. Wang, Z. Feng, P. Cui, W. Zhu, Y. Gong, M.-A. Girard, G. Lajoie, J. Trottier, Q. Zhang, L. Gu, Y. Wang, W. Zuo, Y. Yang, J. B. Goodenough and K. Zaghib, *Nat. Commun.*, 2021, **12**, 13.

22 T. Yuan, Y. Sun, S. Li, H. Che, Q. Zheng, Y. Ni, Y. Zhang, J. Zou, X. Zang, S.-H. Wei, Y. Pang, S. Xia, S. Zheng, L. Chen and Z.-F. Ma, *Nano Res.*, 2023, **16**, 6890–6902.

23 Q. Mao, Y. Yu, J. Wang, L. Zheng, Z. Wang, Y. Qiu, Y. Hao and X. Liu, *J. Mater. Chem. A*, 2021, **9**, 10803–10811.

24 Z. Cheng, B. Zhao, Y.-J. Guo, L. Yu, B. Yuan, W. Hua, Y.-X. Yin, S. Xu, B. Xiao, X. Han, P.-F. Wang and Y.-G. Guo, *Adv. Energy Mater.*, 2022, **12**, 2103461.

25 R. J. Clément, J. Xu, D. S. Middlemiss, J. Alvarado, C. Ma, Y. S. Meng and C. P. Grey, *J. Mater. Chem. A*, 2017, **5**, 4129–4143.

26 J. Xu, D. H. Lee, R. J. Clément, X. Yu, M. Leskes, A. J. Pell, G. Pintacuda, X.-Q. Yang, C. P. Grey and Y. S. Meng, *Chem. Mater.*, 2014, **26**, 1260–1269.

27 G. Singh, N. Tapia-Ruiz, J. M. Lopez del Amo, U. Maitra, J. W. Somerville, A. R. Armstrong, J. Martinez de Ilarduya, T. Rojo and P. G. Bruce, *Chem. Mater.*, 2016, **28**, 5087–5094.

28 N. Tapia-Ruiz, W. M. Dose, N. Sharma, H. Chen, J. Heath, J. W. Somerville, U. Maitra, M. S. Islam and P. G. Bruce, *Energy Environ. Sci.*, 2018, **11**, 1470–1479.

29 H. Hou, B. Gan, Y. Gong, N. Chen and C. Sun, *Inorg. Chem.*, 2016, **55**, 9033–9037.

30 X. Wu, G.-L. Xu, G. Zhong, Z. Gong, M. J. McDonald, S. Zheng, R. Fu, Z. Chen, K. Amine and Y. Yang, *ACS Appl. Mater. Interfaces*, 2016, **8**, 22227–22237.

31 I. Hasa, S. Passerini and J. Hassoun, *J. Mater. Chem. A*, 2017, **5**, 4467–4477.

32 N. Yabuuchi, M. Kajiyama, J. Iwatate, H. Nishikawa, S. Hitomi, R. Okuyama, R. Usui, Y. Yamada and S. Komaba, *Nat. Mater.*, 2012, **11**, 512–517.

33 D. Yuan, X. Hu, J. Qian, F. Pei, F. Wu, R. Mao, X. Ai, H. Yang and Y. Cao, *Electrochim. Acta*, 2014, **116**, 300–305.

34 L. Wang, Y.-G. Sun, L.-L. Hu, J.-Y. Piao, J. Guo, A. Manthiram, J. Ma and A.-M. Cao, *J. Mater. Chem. A*, 2017, **5**, 8752–8761.

35 D. Buchholz, A. Moretti, R. Kloepsch, S. Nowak, V. Siozios, M. Winter and S. Passerini, *Chem. Mater.*, 2013, **25**, 142–148.

36 H. Yoshida, N. Yabuuchi, K. Kubota, I. Ikeuchi, A. Garsuch, M. Schulz-Dobrick and S. Komaba, *Chem. Commun.*, 2014, **50**, 3677–3680.

37 S. Yuan, J. Qi, M. Jiang, G. Cui, X.-Z. Liao, X. Liu, G. Tan, W. Wen, Y.-S. He and Z.-F. Ma, *ACS Appl. Mater. Interfaces*, 2021, **13**, 3793–3804.

38 L. Xue, J.-z Wang, Y.-x Teng, J.-l Lu and S. Bao, *Mater. Lett.*, 2021, **303**, 130507.

39 Y. Huang, Z. Yan, W. Luo, Z. Hu, G. Liu, L. Zhang, X. Yang, M. Ou, W. Liu, L. Huang, H. Lin, C.-T. Chen, J. Luo, S. Li, J. Han, S. Chou and Y. Huang, *Energy Storage Mater.*, 2020, **29**, 182–189.

40 X. Xu, Q. Liu, H. Zhu, S. Cao and Y. Liu, *ACS Sustainable Chem. Eng.*, 2023, **11**, 15006–15019.

41 H. Zhang and J. F. Banfield, *J. Mater. Chem.*, 1998, **8**, 2073–2076.

42 P. Bai, D. A. Cogswell and M. Z. Bazant, *Nano Lett.*, 2011, **11**, 4890–4896.

43 N. Meethong, H.-Y. S. Huang, W. C. Carter and Y.-M. Chiang, *Electrochem. Solid-State Lett.*, 2007, **10**, A134.

44 J. S. Corsi, A. K. Ng, Y. Huang and E. Detsi, *ACS Appl. Energy Mater.*, 2022, **5**, 4547–4555.

45 Y. Liu, Q. Shen, X. Zhao, J. Zhang, X. Liu, T. Wang, N. Zhang, L. Jiao, J. Chen and L.-Z. Fan, *Adv. Funct. Mater.*, 2020, **30**, 1907837.

46 P. G. Bruce, B. Scrosati and J.-M. Tarascon, *Angew. Chem., Int. Ed.*, 2008, **47**, 2930–2946.